Inorganic Chemistry
Article
pubs.acs.org/IC

Guest-Effected Spin-Crossover in a Novel Three-Dimensional Self-Penetrating Coordination Polymer with Permanent Porosity

Jin-Yan Li, Zheng Yan, Zhao-Ping Ni,* Ze-Min Zhang, Yan-Cong Chen, Wei Liu, and Ming-Liang Tong*

Key Laboratory of Bioinorganic and Synthetic Chemistry of Ministry of Education, State Key Laboratory of Optoelectronic Materials and Technologies, School of Chemistry and Chemical Engineering, Sun Yat-Sen University, Guangzhou 510275, People's Republic of China

Ⓢ *Supporting Information*

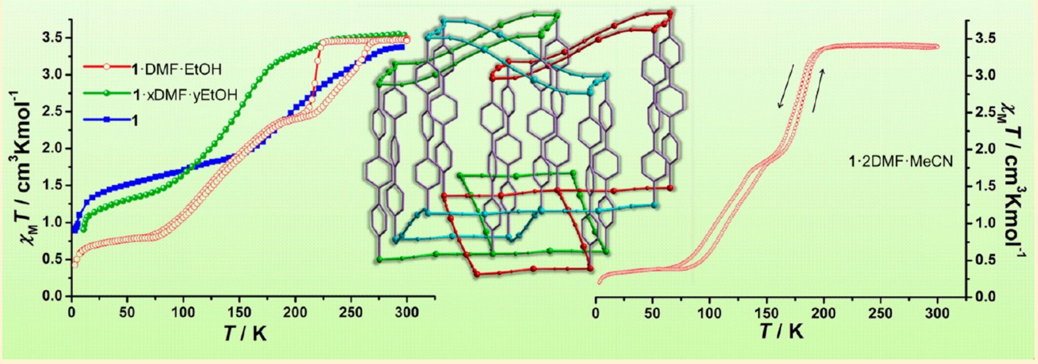

ABSTRACT: Porous and nonporous 3D heterobimetallic coordination polymers based on the 1,4-di(pyridin-4-yl)benzene ligand (dpb), $[Fe(dpb)\{Ag(CN)_2\}\{Ag_2(CN)_3\}]\cdot n$Solv (**1**·*n*Solv; *n*Solv = DMF·EtOH, 2DMF·MeCN) and $[Fe(dpb)_2\{Ag(CN)_2\}_2]$ (**2**), have been synthesized by diffusion technique, respectively. Single-crystal X-ray analysis shows that **1**·*n*Solv consists of a 3D self-penetrating network with in-situ-generated $[Ag_2(CN)_3]^-$ species and displays one of the largest volume values of porosity (299 Å^3 per iron atom) after desolvation for the Hoffman-like porous SCO coordination polymers to date. In contrast, nonporous compound **2** is composed of two independent interpenetrated 3D nets with in-situ-generated $[Ag(dpb)(CN)_2]^-$ species. Their significant distinctions of structural architectures lead to dramatically different magnetic properties: **1**·*n*Solv displays two-step guest-effected SCO with hysteresis, whereas **2** presents characteristic paramagnetic behavior.

■ INTRODUCTION

The spin crossover (SCO) phenomenon associated with the electronic rearrangement for octahedral d^4−d^7 transition metals represents a prototypical example of molecular switching.[1] For instance, the iron(II) ion with a d^6 electronic configuration may switch between the paramagnetic high-spin state and the diamagnetic low-spin state by external perturbations, such as temperature, pressure, irradiation, or magnetic fields.[1,2] Then, they are promising for potential applications in switching, data storage, display devices, and sensors.[3] Depending on the nature of ligands, crystal packing, solvent molecules, and uncoordinating counterions, fine-tuning SCO properties for these compounds to have any real technological impact has been actively investigated for a long time.[4]

In recent decades, many researchers have focused on investigating synergies between host−guest chemistry and SCO behavior in Fe^{II}-containing 2D and 3D porous coordination polymers where the guest species may perturb the geometry and electronic environment of SCO centers.[5] Typical systems of the 2D porous SCO coordination polymers have the general formula $[Fe(L)_2(NCS)_2]\cdot$guest (L represents a bis-monodentate pyridine-like ligand), which consist of doubly interpenetrating rhombic grids defining one-dimensional channels.[5a,6] In regard to the 3D porous SCO coordination polymers, the most representative series are well-known Hoffman clathrates $[Fe(L)\{M^{II}(CN)_4\}]\cdot$Guest[5b,7] (where L is the same as that mentioned above, M^{II} may be Ni, Pd, or Pt) and dicyanoargentate/dicyanoaurate derivatives including a $[Fe\{M^I(CN)_2\}_2]_\infty$ polymeric moiety.[8] A significant aspect of these series concerns the porosity (the volume value of porosity per iron atom). Considering this volume value, we compared a list of Hoffman porous SCO coordination polymers $[Fe(L)\{M^{II}(CN)_4\}]$ in which L = pyrazine (90 Å^3),[9] 4,4′-azopyridine (286 Å^3),[10] 1,2-di(4-pyridyl)ethylene (272.4 Å^3),[7f] and bis(4-pyridyl)acetylene (293 Å^3).[11] Moreover, the first dicyanoargentate/dicyanoaurate derivatives displaying permanent porosity (240 Å^3), $[Fe(TPT)_{2/3}\{M^I(CN)_2\}_2]\cdot n$Solv, TPT = 2,4,6-tris(4-pyridyl)-1,3,5-triazine, have been reported recently.[8c] These Hoffman-like porous systems mentioned above can include large guests (naphthalene, anthracene, phenazine), conferring a more cooperative SCO behavior in correlation to

Received: December 13, 2013
Published: March 31, 2014

Table 1. Crystal Data and Refinement Parameters for **1**·DMF·EtOH and **2**

	1·DMF·EtOH			**2**
T [K]	273(2)	180(2)	150(2)	150(2)
empirical formula	$C_{26}H_{25}N_8O_2Ag_3Fe$	$C_{26}H_{25}N_8O_2Ag_3Fe$	$C_{26}H_{25}N_8O_2Ag_3Fe$	$C_{36}H_{24}Ag_2FeN_8$
fw	861.00	861.00	861.00	840.22
cryst syst	orthorhombic	orthorhombic	orthorhombic	monoclinic
space group	*Pcca*	*Pcca*	*Pcca*	$P2_1/n$
a [Å]	12.0545(4)	12.0015(5)	12.0144(4)	8.838(2)
b [Å]	17.2800(6)	17.0849(8)	16.9892(6)	16.380(4)
c [Å]	31.6186(9)	31.3706(16)	31.2716(13)	12.421(4)
β [deg]	90	90	90	108.642(4)
V [Å^3]	6586.2(4)	6432.4(5)	6383.0(4)	1703.6(9)
Z	8	8	8	2
ρ_{calcd} (mg cm^{-3})	1.737	1.778	1.792	1.638
$F(000)$	3360	3360	3360	832
μ(Cu Kα/Mo Kα) (mm^{-1})	17.849	18.276	18.417	1.596
cryst size (mm)	0.33 × 0.30 × 0.06	0.17 × 0.12 × 0.04	0.33 × 0.30 × 0.06	0.20 × 0.11 × 0.08
$R_1[I > 2\sigma(I)]$	0.0774 (SQUEEZE)	0.0694 (SQUEEZE)	0.0948	0.0333
$wR[I > 2\sigma(I)]$	0.2060 (SQUEEZE)	0.1869 (SQUEEZE)	0.2454	0.0801
S	0.920	0.996	1.095	1.050

guest sorption/desorption and varieties. As further research, we have chosen a more rigid and longer linear bridging ligand, 1,4-di(pyridin-4-yl)benzene (dpb), in order to obtain novel Hoffman-like SCO coordination polymers with large porosity.

Here we report two novel 3D heterobimetallic coordination polymers based on the 1,4-di(pyridin-4-yl)benzene ligand. They are formulated as $[Fe(dpb)\{Ag(CN)_2\}\{Ag_2(CN)_3\}]\cdot n$Solv (**1**·*n*Solv; *n*Solv = DMF·EtOH, 2DMF·MeCN) and $[Fe(dpb)_2\{Ag(CN)_2\}_2]$ (**2**). Interestingly, **1**·*n*Solv contains a $[Ag_2(CN)_3]^-$ motif in-situ generated, which has been only reported twice in Hoffman-like SCO coordination polymers.[12] It can be simplified as two types of new topological nets with one of the largest volume values of porosity (299 Å per iron atom) in Hoffman-like porous SCO coordination polymers. On the other hand, in-situ generation of $[Ag(dpb)(CN)_2]^-$ is observed in compound **2**. Concerning the magnetic properties, guest-effected SCO versus high-spin state phenomena are shown in **1**·*n*Solv and **2**, respectively, in which **1**·DMF·EtOH and **1**·2DMF·MeCN display two-step spin crossover behaviors.

■ EXPERIMENTAL SECTION

Materials and General Procedures. All of the reagents used in this work were obtained from commercial sources. Magnetic susceptibility measurements were performed on a Quantum Design PPMS instrument operating under a field of 1000 Oe. The diamagnetic correction for each sample was determined from Pascal's constants. C, H, and N microanalyses were performed on fresh sample, which was taken out immediately from the mother liquor, with an Elementar Vario-EL CHN elemental analyzer. FT-IR spectra were recorded in KBr tablets in the range 4000−400 cm^{-1} on a Bio-Rad FTS-7 spectrometer. Thermogravimetric (TG) analysis was carried out on a NETZSCH TG209F3 thermogravimetric analyzer. X-ray powder diffraction (XPRD) intensities were measured at 293 K on a Bruker D8 Advance diffractometer (Cu Kα, λ = 1.54056 Å) by scanning over the range of 3−50° with a step of 0.2°/s. A simultaneous TG-DTA coupled to a mass spectrometer (STA449 F3 Jupiter-QMS 403C aedo) was used to analyze the chemical nature of the guest molecules.

*Synthesis. $[Fe(dpb)\{Ag(CN)_2\}\{Ag_2(CN)_3\}]\cdot$DMF·EtOH (**1**·DMF·EtOH).* Single crystals of **1**·DMF·EtOH were obtained by the slow diffusion technique. $K[Ag(CN)_2]$ (30 mg, 0.15 mmol) and dpb (12 mg, 0.05 mmol) dissolved in DMF (5 mL) were placed in a 5 mL test tube. While a 1 mL test tube contained a solution of $Fe(ClO_4)_2\cdot 9H_2O$ (21 mg, 0.05 mmol) in EtOH (1 mL). The two vessels were then inserted into a 30 mL vial filled with EtOH. Light yellow plate crystals suitable for single-crystal X-ray diffraction (SCXRD) were formed after 2 weeks. Yield: about 70%. Anal. Calcd for $C_{26}H_{25}N_8O_2Ag_3Fe$: C, 36.27; H, 2.93; N, 13.01. Found: C, 36.05; H, 2.82; N, 13.11. IR data for **1**·DMF·EtOH (KBr, cm^{-1}): $\tilde{\nu}$ = 3413 (m), 3074 (w), 3041 (w), 2915 (m), 2871 (w), 2157 (s), 2104 (m), 1675 (s), 1604 (s), 1548 (m), 1484 (s), 1430 (m), 1382(s), 1091 (s), 1062 (w), 811 (s), 720 (s).

*$[Fe(dpb)\{Ag(CN)_2\}\{Ag_2(CN)_3\}]\cdot$2DMF·MeCN (**1**·2DMF·MeCN).* This compound was synthesized by means of layer diffusion. A solution of $K[Ag(CN)_2]$ (30 mg, 0.15 mmol) and dpb (12 mg, 0.05 mmol) in DMF (5 mL) was placed at the base of a test tube. In addition, $Fe(ClO_4)_2\cdot 9H_2O$ (21 mg, 0.05 mmol) dissolved in MeCN (4 mL) was layered above the buffer layer of a mixture of MeCN (4 mL) and DMF (2 mL). Light yellow plate crystals were obtained after 1 week. Yield: about 70%. Anal. Calcd for $C_{29}H_{29}N_{10}O_2Ag_3Fe$: C, 37.49; H, 3.15; N, 15.08. Found: C, 37.15; H, 3.52; N, 15.37. IR data for **1**·2DMF·MeCN (KBr, cm^{-1}): 3056 (m), 3030 (w), 2927 (m), 2163 (s), 2065 (m), 1663 (s), 1607 (s), 1550 (m), 1484 (s), 1428 (m), 1386 (s), 1092 (m), 1068 (w), 809 (s), 717 (s).

*$[Fe(dpb)_2\{Ag(CN)_2\}_2]$ (**2**).* Single crystals of **2** were formed by the slow diffusion technique. $K[Ag(CN)_2]$ (20 mg, 0.10 mmol) and dpb (12 mg, 0.05 mmol) dissolved in DMF (5 mL) were placed in a 5 mL test tube. A 1 mL test tube contained a solution of $Fe(ClO_4)_2\cdot 9H_2O$ (21 mg, 0.05 mmol) in EtOH (1 mL). The two vessels were then inserted into a 30 mL vial filled with EtOH. Orange block crystals suitable for single-crystal X-ray diffraction (SCXRD) were obtained after 2 weeks. However, a few light yellow plate crystals, **1**·DMF·EtOH, were also collected at the same time. Yield: about 50%. Anal. Calcd for $C_{36}H_{24}N_8Ag_2Fe$: C, 51.46; H, 2.88; N, 13.34. Found: C, 51.33; H, 2.95; N, 13.13. IR data for **2** (KBr, cm^{-1}): 3073 (w), 3037 (m), 2923 (w), 2144 (s), 2074 (w), 1600 (s), 1548 (m), 1496 (s), 1425 (m), 1398 (m), 1045 (w), 808 (s), 712 (s).

X-ray Crystallography. Diffraction intensities of **1**·DMF·EtOH were collected on an Oxford Diffraction Gemini R CCD diffractometer with Cu Kα radiation (λ = 1.54178 Å) at 150(2), 180(2), and 273(2) K. Intensity data of **2** were recorded on a Rigaku R-AXIS SPIDE IP system with Mo Kα radiation. Structures were solved by direct methods, and all non-hydrogen atoms were refined anisotropically by least-squares on F^2 using the SHELXTL program. Hydrogen atoms on organic ligands were generated by the riding mode.[13] For **1**·DMF·EtOH, the disordered DMF and ethanol molecules could not be modeled properly; thus, the program SQUEEZE,[14] a part of the PLATON package of crystallographic

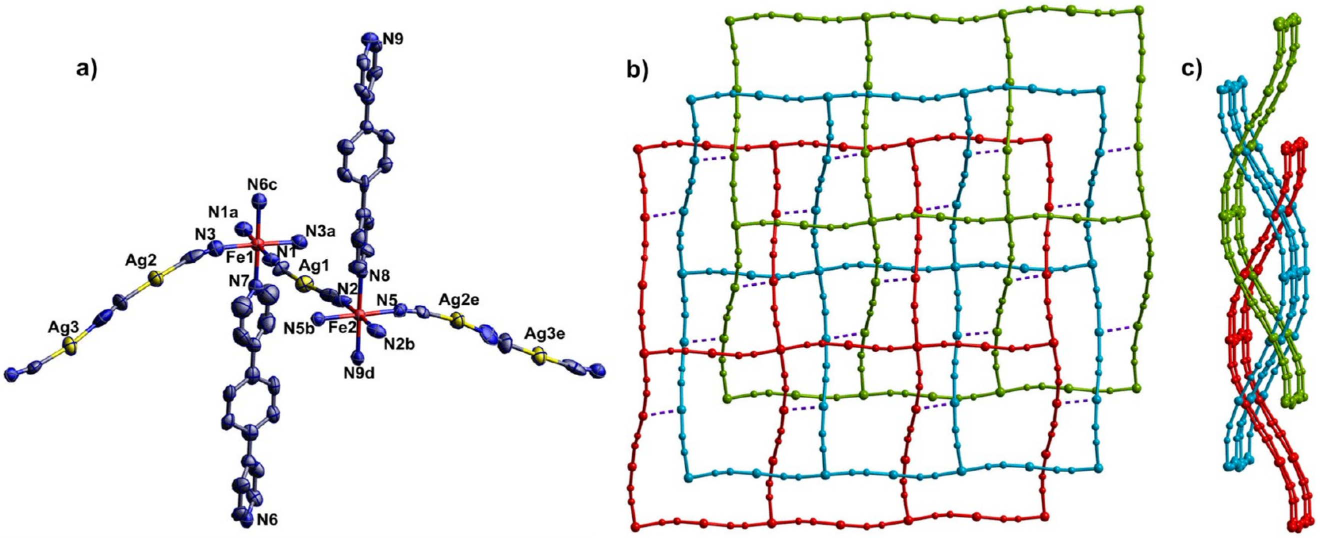

Figure 1. (a) Coordination environments of the two crystallographically independent Fe atoms in **1**·DMF·EtOH. Symmetry codes: (a) $-x - 3/2, -y, z$; (b) $-x - 1/2, -y + 1, z$; (c) $-x - 3/2, y, z - 1/2$; (d) $-x - 1/2, y, z + 1/2$; (e) $x + 3/2, y, -z + 1$; (b and c) Two views of the same fragment of **1**·DMF·EtOH, which emphasize the argentophilic interactions involving Ag atoms of $[Ag_2(CN)_3]^-$ and the interweaved way of $\{Fe[Ag(CN)_2][Ag_2(CN)_3]\}_\infty$ triple layers.

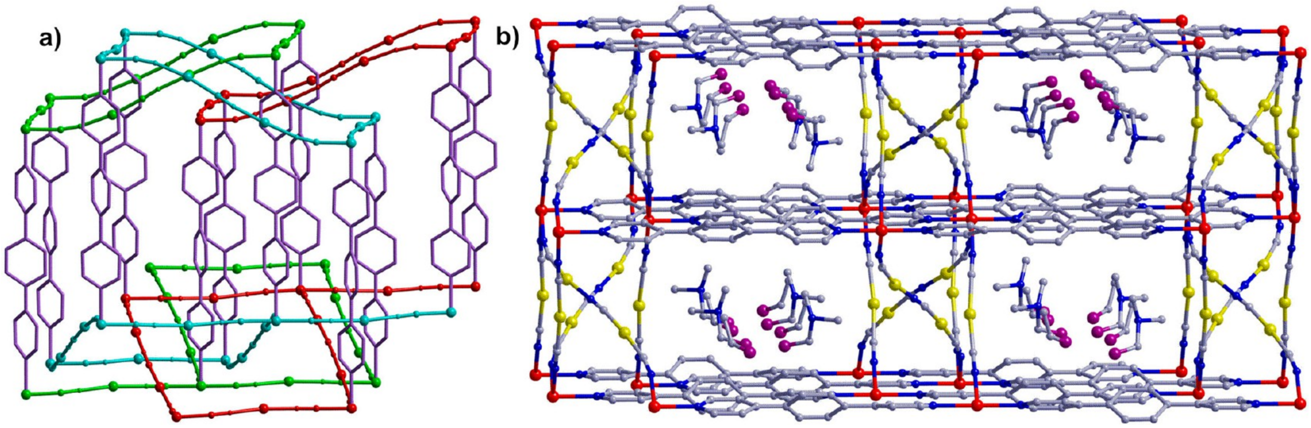

Figure 2. (a) Fragment of **1**·DMF·EtOH showing a self-penetrating network. (b) View of a fragment of the clathrate compound **1**·DMF·EtOH, which illustrates the 1D open channels along the *a* axis and alternate location of guest molecules (DMF and EtOH). Hydrogen atoms have been omitted for clarity. Fe, red; Ag, yellow; O, purple; N, blue; C, gray.

software, was used to calculate the solvent disorder area and remove its contribution to the overall intensity data.

CCDC-967869 (**1**_150K), CCDC-967870 (**1**_180K), CCDC-967871 (**1**_273K), and CCDC-967872 (**2**_150K) contain supplementary crystallographic data for this paper. These data can be obtained free of charge from The Cambridge Crystallographic Data Centre via www.ccdc.cam.ac.uk/data_request/cif.

■ RESULTS AND DISCUSSION

Single-Crystal X-ray Structures. Compounds **1**·*n*Solv and **2** have been synthesized by the slow diffusion technique. Crystal structure determinations of compound **1**·DMF·EtOH were performed at 150, 180, and 273 K. This compound adopts orthorhombic space group *Pcca* whatever the temperature. Details of the single-crystal refinement for **1**·DMF·EtOH are shown in Table 1. A selection of bond lengths and angles is given in Table S1, Supporting Information. The structure of **1**·DMF·EtOH consists of an intricate 3D framework and consists of two types of crystallographically independent iron atoms. With Fe1 and Fe2 located on inversion centers, there is one iron atom in the asymmetric unit. The iron atom lies at the center defining a distorted octahedral [FeN6] site. Figure 1a displays the coordination environments of the two iron centers. The equatorial positions are occupied by four cyanide nitrogen atoms belonging to $[Ag(CN)_2]^-$ and $[Ag_2(CN)_3]^-$, while the remaining axial positions are occupied by the nitrogen atoms of the dpb organic ligands. At 273 K, the average Fe1−N and Fe2−N bond lengths (⟨Fe1−N⟩ and ⟨Fe2−N⟩) are 2.17 and 2.18 Å, respectively, suggesting both of the Fe^{II} ions are in the HS states. At 150 K, they are 2.08 and 2.06 Å, respectively, clearly indicating the presence of a HS ↔ LS spin transition.

Given the intricate structure of **1**·DMF·EtOH, we deconstructed the network in several significant fragments. Coordination of the iron centers to the $[Ag(CN)_2]^-$ and $[Ag_2(CN)_3]^-$ groups leads to formation of a $\{Fe[Ag(CN)_2]-[Ag_2(CN)_3]\}_\infty$ layer as shown in Figure 1b, in which two types of iron atoms (Fe1 and Fe2) are situated alternately to form $\{[FeAg(CN)_2]_2[FeAg_2(CN)_3]_2\}$ rectangular grids. Interestingly, the three closest layers can be organized as one group (Figure 1b), in which there exists significant argentophilic

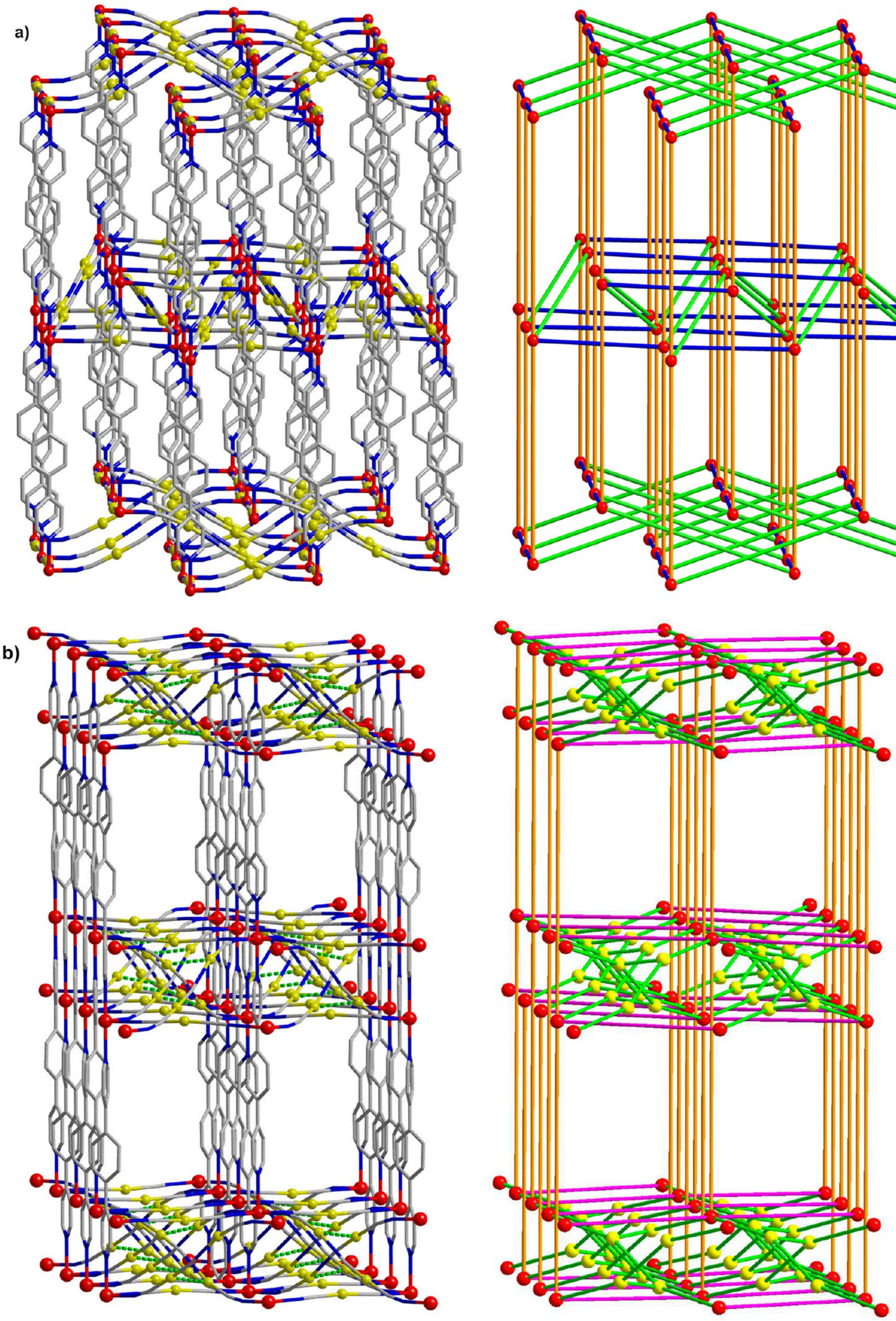

Figure 3. View of a portion of the 3D framework in **1**·DMF·EtOH and corresponding topological networks. (a) New 6-connected net with the Schläfli symbol of $(4^4.6^{11})$ when the Fe atom is defined as a node. (b) Another new (3,6)-connected net with the Schläfli symbol of $(6.8^2)_2(6^9.8^6)$ when Fe, Ag2, and Ag3 are defined as nodes.

interactions for $[Ag_2(CN)_3]^-$ between the adjacent layers, whereas no argentophilic interaction is observed involving $[Ag(CN)_2]^-$. On the other hand, the layers are waved and the iron atoms in each layer are not coplanar, as the $[Ag_2(CN)_3]^-$

units are bent-like S type. Consequently, the triple layers interweave with each other up and down along the $[Ag_2(CN)_3]^-$ direction. Furthermore, as depicted in Figure 2a, the dpb ligands bridge iron atoms belonging to the adjacent two consecutive triple layers leading to an open 3D self-penetrating network.[12a,15] The topological network is analyzed by the Topos program[16] as shown in Figure 3. The results exhibit two types of new topological nets depending on whether you take into account the argentophilic interactions. (1) In the case of ignoring the argentophilic interactions, the dpb organic ligands, $[Ag(CN)_2]^-$ and $[Ag_2(CN)_3]^-$ groups can be viewed as connectors, while Fe atoms are reduced into 6-connected nodes. The Schläfli symbol for this uninodal net can be described as $(4^4.6^{11})$. (2) When considering the argentophilic interactions, Fe atoms and Ag atoms belonging to $[Ag_2(CN)_3]^-$ groups are defined as 6-connected and 3-connected nodes, respectively. Consequently, it generates a new (3,6)-connected net with the Schläfli symbol of $(6.8^2)_2(6^9.8^6)$. The pillared topology leads to 1D open channels along the *a* direction, where DMF and EtOH molecules are situated alternately (see Figure 2b). There exists a void space that represents 37.5% (2394.7 Å) of the unit-cell volume at 150 K when removing the solvent molecules, which is 299 Å^3 per iron atom.[14]

Single crystals of **1**·2DMF·MeCN deteriorated significantly as soon as leaving away from the mother liquor and changed to a polymorph. Unfortunately, many attempts to obtain single crystals suitable for performing X-ray determinations failed. Thus, depending on the X-ray powder diffraction, TG-MS experiments, and elemental analysis, we conclude that its framework is identical with **1**·DMF·EtOH, while the guest molecules are MeCN and DMF instead (Figures S1 and S2, Supporting Information).

Compound **2** crystallizes in the monoclinic $P2_1/c$ space group at 150 K. Selected crystallographic data and bond lengths and angles are listed in Tables 1 and S2, Supporting Information, respectively. The crystal structure of **2** is closely relevant to the reported compounds $[Fe^{II}(L)_2\{Ag(CN)_2\}_2]$ (L = 4,4′-bipyridine (**A**), bispyridylethylene (**B**), and 4,4′-bis(pyridyl)acetylene (**C**).[17] All iron atoms are crystallographically equivalent and situated in the middle of a distorted octahedron that is defined by the $[FeN_6]$ sphere as shown in Figure 4. The equatorial positions are occupied by four $[Ag(CN)_2]^-$ groups, while the remaining axial positions are occupied by two dpb ligands. The average Fe−N bond length of 2.19 Å is indicative of HS states of iron centers. Coordination of iron centers to the $[Ag(CN)_2]^-$ groups leads to formation of corrugated layers $\{Fe[Ag(CN)_2]_2\}_\infty$. The dpb ligands coordinated to iron atoms of one sheet thread the meshes of the immediately adjacent sheet and bind to the silver atoms of the subsequent 2D network (Figure 5), which defines two independent interpenetrated 3D nets. Consequently, no significant void space in the structure is observed. As depicted in Figure S3, Supporting Information, the framework can be topologically represented as a (3,6)-connected rutile net with the Schläfli symbol of $(4.6^2)_2(4^2.6^{10}.8^3)$, in which the 1,4-dpb ligands and CN groups are viewed as connectors while Fe and Ag atoms are reduced into 6-connected and 3-connected nodes.

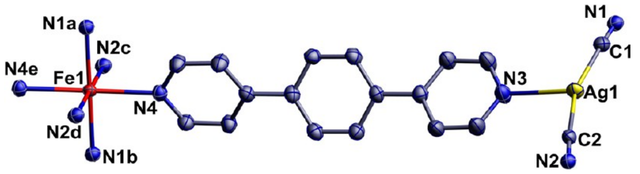

Figure 4. View of a representative fragment of **2** showing the coordination environment of the Fe atom. Symmetry codes: (a) −*x* − 1, −*y*, −*z* + 1; (b) *x* − 1, *y*, *z* + 1; (c) −*x* − 1/2, *y* − 1/2, −*z* + 3/2; (d) *x* − 3/2, −*y* + 1/2, *z* + 1/2; (e) −*x* − 2, −*y*, −*z* + 2.

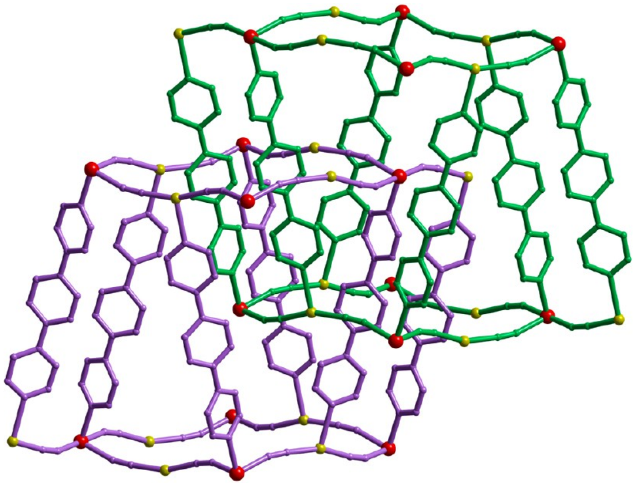

Figure 5. View of the 2-fold interpenetrated frameworks of **2**. Fe, red; Ag, yellow; net 1, green; net 2, purple.

Magnetic Properties. The magnetic property of **1**·DMF·EtOH is depicted in the form of χ_MT versus T (χ_M is the molar magnetic susceptibility and T is the temperature) as shown in Figure 6. For the fresh sample soaked in mother liquor, the value of χ_MT is 3.49 cm^3 K mol^{-1} at 300 K, which is in the range of the values expected for an iron(II) ion in the HS state. As the temperature is lowered, χ_MT remains almost constant down to 225 K and begins to decrease more rapidly, defining a relatively abrupt spin transition that ends in an inclined plateau centered at 195 K with $\chi_MT \approx 2.41$ cm^3 K mol^{-1}. In this high-temperature step, the warming procedure denotes the occurrence of an asymmetric hysteresis loop ca. 27 K wide, and the corresponding critical temperatures are $T_c^{1\downarrow}$ = 218 K and $T_c^{1\uparrow}$ =245 K, respectively. The variations of χ_MT for this step demonstrate that around 31% of iron centers take place spin transition. For the temperature below 195 K, χ_MT experiences a quite smooth drop. This gradual spin transition without detectable hysteresis ends in an inclined plateau centered at 43 K with $\chi_MT \approx 0.75$ cm^3 K mol^{-1}, which denotes that around 21% of the iron centers remain in the HS state, and the critical temperature is 131 K. In regard to the decrease of χ_MT below 43 K, it is ascribed to the zero-field splitting of the paramagnetic iron centers. Moreover, measurement of a second cycle is nearly identical with that of the first cycle (Figure S4, Supporting Information).

Interestingly, the measurement for the sample without mother liquor displays an even more incomplete and gradual one-step spin transition without hysteresis, in which all iron centers are in the HS states at 300 K and about 60% iron species change the spin states down to 77 K (T_c = 150 K). The differences of the SCO behaviors mentioned above suggest that the loosely attached solvent molecules play a significant role in determining the magnetic behavior of the porous coordination polymer. Thus, we try to measure the magnetic properties of the desolvated sample **1**, which is obtained by heating **1**·DMF·EtOH under N_2 at 160 °C for 30 min. The preserved

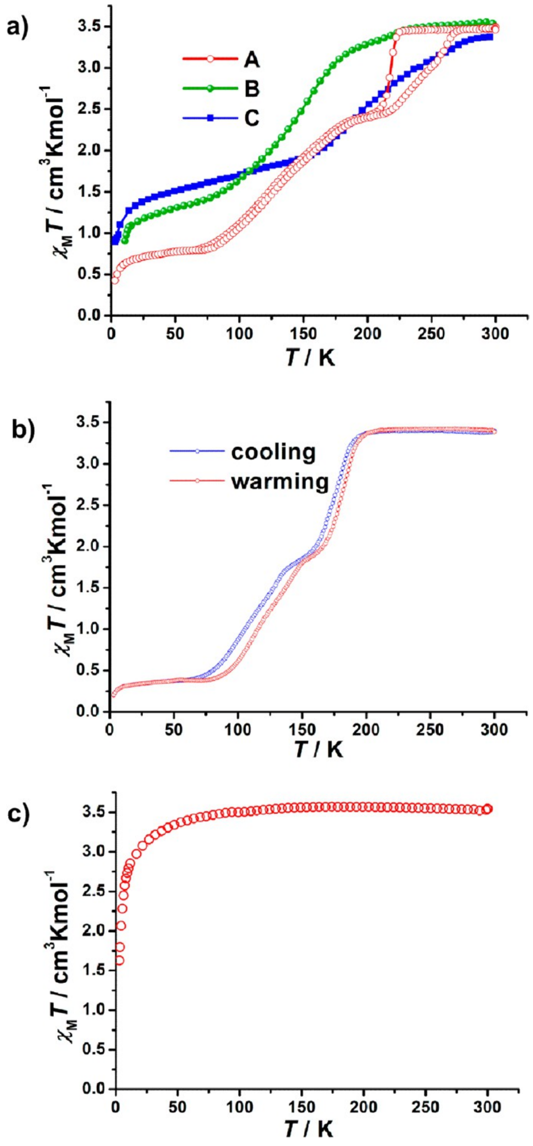

Figure 6. (a) Temperature dependence of $\chi_M T$ for **1**·DMF·EtOH soaked in mother liquor (A), partially desorbed sample of **1**·DMF·EtOH (B), and desorbed analogue **1** (C). (b) Magnetic properties in the form of $\chi_M T$ versus T for **1**·2DMF·MeCN. (c) Temperature dependence of $\chi_M T$ for **2**.

framework after heating is proven by X-ray powder diffraction (see Figure S1, Supporting Information), denoting the presence of the permanent porosity. As shown in Figure 6a, $\chi_M T$ of **1** is equal to 3.37 cm^3 K mol^{-1} at 300 K. As the temperature is lowered it undergoes a gradual half-spin transition, which ends in an inclined plateau centered at 102 K with $\chi_M T$ = 1.72 cm^3 K mol^{-1}. The critical temperature is 206 K. With further cooling, $\chi_M T$ decreases again due to the zero-field splitting of the remaining ca. 50% HS species.

In order to further explore the guest-effected spin-crossover behavior, the magnetic susceptibility of **1**·2DMF·MeCN was measured. $\chi_M T$ is equal to 3.40 cm^3 K mol^{-1} at 300 K and remains constant down to 205 K. Below this temperature, it undergoes a relatively cooperative two-step spin transition ($T_c^{1\downarrow}$ = 175 K and $T_c^{2\downarrow}$ = 109 K) in which each step nearly involves 50% conversion of iron centers. This spin transition exhibits 6 and 10 K hysteresis width with critical temperatures $T_c^{1\uparrow}$ = 181K and $T_c^{2\uparrow}$ = 119 K in the warming procedure. This spin transition ends in a plateau centered at 35 K with $\chi_M T$ = 0.35 cm^3 K mol^{-1}, which indicates a few residual HS iron centers. In addition, measurement of the second cycle is nearly identical with that of the first cycle (Figure S4, Supporting Information). Since the loosely attached guest molecules release quite easily, we were unable to carry out the DSC measurements for **1**·2DMF·MeCN and **1**·DMF·EtOH.

In contrast to the SCO behavior of compounds **1**·*n*Solv, the HS state is observed for compound **2**. The $\chi_M T$ value is equal to 3.52 cm^3 K mol^{-1} at 300 K and remains constant down to 75 K. Below this temperature, $\chi_M T$ decreases rapidly owning to the zero-field splitting.

It is well known that guest molecules may induce dramatic changes in the SCO behavior by subtle electronic effects and/or structural modifications.[7f] As the guest molecules are relatively thermally disordered for **1**·*n*Solv, it is difficult to illustrate the roles of the guest molecules with respect to the host−guest interactions. However, it is safe to say that the presence of the guest molecule results in a more cooperative spin-transition behavior. Both **1**·DMF·EtOH and **1**·2DMF·MeCN undergo two-step SCO with a hysteresis loop, while the partially desolvated sample and desorbed analogue **1** display more incomplete and gradual one-step SCO. With regard to the variation of T_c values of **1**·DMF·EtOH and **1**·2DMF·MeCN, first, we may turn our attention to the subtle electronic influence of different guest molecules, which is quantified in the bulk by the dielectric constant, ε (which concerns both the polarity and the polarizability), as illustrated in compounds [Fe(NCS)$_2$(bpbd)$_2$]·guest (bpbd = 2,3-bis(4′-pyridyl)-2,3-butanediol) by Kepert et al.[6e] Considering the correlation between T_c and dielectric constant ε, which may indicate a second-coordination sphere effect where framework polarization effects have an impact on the ligand field energies, a smaller ε value is in favor of the LS state. The T_c values of **1**·DMF·EtOH (ε(EtOH) = 24.3) are higher than that of **1**·2DMF·MeCN (ε(MeCN) = 37.5), which is consistent with the trend mentioned above. Second, the sizes and numbers of the guest molecules are different between **1**·2DMF·MeCN and **1**·DMF·EtOH, in which the former is relatively larger. Therefore, the down-shift tendency of the T_c from **1**·DMF·EtOH to **1**·2DMF·MeCN can also be rationalized by an internal pressure effect in which the larger guest molecules prefer to stabilize the HS species.[7b]

In further structure-magneto studies on the two-step SCO behavior of **1**·DMF·EtOH, deep insight into the crystal structure was investigated. At first glance, the average ⟨Fe−N⟩ distances for two nonequivalent iron centers are very similar at 273 K. However, the structural parameters around Fe1 and Fe2 are actually different (see Table 2). First, the octahedral distortion parameter[18] ($\sum$Fe1 = 13.8° and $\sum$Fe2 = 7.2° at 273 K) are different, suggesting the more distorted coordination environment of Fe1 than that of Fe2. Second, the pillared ligands connecting two equivalent iron centers differ in steric configurations for Fe1 and Fe2 as shown in Table 2. The two pyridine rings in the dpb ligand linking two Fe1 ions are nearly in one plane, while the dihedral angle of the two pyridine rings in the dpb ligand linking two Fe2 ions is 19.73° at 273 K. The dihedral angles of the phenyl ring with each pyridine ring in the dpb ligand are also different for Fe1 and Fe2. Then these structural differences may result in different ligand field strengths in sites Fe1 and Fe2. Upon lowing the temperature the unit-cell volume, the ⟨Fe−N⟩ distance, the Fe···Fe distance linked by dbp and [Ag(CN)$_2$]$^-$, and the argentophilic

Table 2. Selected Interatomic Distances [Angstroms] and Angles [degrees] for **1**·DMF·EtOH and **2**

	1·DMF·EtOH			**2**
T [K]	273	180	150	150
⟨Fe1−N⟩	2.19	2.14	2.08	2.19
⟨Fe2−N⟩	2.18	2.13	2.08	
∑Fe1[a]	13.8	12.4	17.0	15.0
∑Fe2[a]	7.2	9.2	10.2	
Fe···Fe[b]	15.809	15.685	15.636	
Fe···Fe[c]	10.535	10.440	10.405	
Ag2···Ag3	3.072	3.038	3.027	
Ag1···Ag2	3.972	3.964	3.948	
Ag1···Ag3	3.473	3.464	3.463	
C2−Ag1−C1	173.1	174.2	174.0	160.6
C3−Ag2−N4	171.4	172.2	171.0	
C4−Ag3−C5	177.2	175.5	176.8	
angle[d]	5.74	4.77	5.21	61.01
angle[e]	37.80/43.54	37.20/41.98	37.35/42.57	32.60/28.43
angle[f]	19.73	15.11	16.72	
angle[g]	45.13/25.39	43.71/28.60	43.89/27.17	

[a]∑ The sum of the deviation of each of the 12 cis angles. [b]The Fe···Fe distance linked by dpb. [c]The Fe···Fe distance linked by $[Ag(CN)_2]^-$. [d]In the dpb linking two Fe1, the dihedral angle of two pyridine rings. [e]In the dpb linking Fe1, the dihedral angles of the phenyl and each pyridine ring. [f]In the dpb linking two Fe2, the dihedral angle of two pyridine rings. [g]In the dpb linking two Fe2, the dihedral angles of the phenyl and each pyridine ring.

interactions are decreased, which is consistent with the spin transition behavior. Although the ⟨Fe−N⟩ distances change simultaneously for Fe1 and Fe2 at 180 and 150 K, the octahedral distortion parameters and bpd configurations show unusual changes with different changing trends as shown in Table 2. Thus, the different extents of the structural changes around Fe1 and Fe2 when decreasing the temperature may provide the possibility of step transition. As the limitation of crystallographic measurements and crystal quality, only an average view of spin states for Fe1 and Fe2 is observed in the plateau temperature. This situation is not unusual in spin-crossover complexes, for example, refs 7e and 19. Since the evidence for symmetry breaking can be very subtle, it is always impossible to detect by a standard laboratory X-ray diffraction. Therefore, a symmetry breaking phase transition cannot be eliminated here.[7g,20]

The huge differences of magnetic behaviors between **1**·*n*Solv and **2** seem to arise from significant differences of structures. For **1**·*n*Solv, the iron centers are ligated with $[Ag_2(CN)_3]^-$ generated in situ and $[Ag(CN)_2]^-$ groups to form $\{Fe[Ag(CN)_2][Ag_2(CN)_3]\}_\infty$ layers, in which strong argentophilic interactions for $[Ag_2(CN)_3]^-$ between two adjacent layers are observed, whereas no significant argentophilic interactions can be found in **2**. Moreover, the C−Ag−C angle in compound **2** is 160.6°, which deviates much from linearity as the Ag atom is coordinated by the dpb ligand. As shown in Table 2, the ⟨Fe−N⟩ of **2** at 150 K is nearly identical with that for **1**·DMF·EtOH at 273 K but significantly longer than that at 150 K. Since the ligand field strength of 10 Dq is proportional to $(1/R)^6$,[21] in which *R* represents the Fe−N distance, the ligand field strength for **2** is smaller than that for **1**·*n*Solv at 150 K. Furthermore, **1**·*n*Solv consists of a more rigid self-penetrating network with strong argentophilic interactions, although it has large permanent porosity with solvent inclusions inside, whereas **2** consists of two independent interpenetrated 3D nets without significant void space. A more significant internal pressure induced by the stronger rigidity of 3D framework may tend to stabilization of the LS state.[11b] In summary, different magnetic behaviors for **1**·*n*Solv and **2** are relevant and reasonable.

Reminiscent of compounds **A**, **B**, and **C**, they are isostructural to **2** with different bridging ligands. However, they also show different magnetic properties. Compounds **2** and **A** show characteristic paramagnetic behavior, while **B** and **C** display spin transition with large thermal hystereses.[17] It clearly suggests that the bridiging ligand has a significant effect on the SCO properties.

CONCLUSIONS

In this work, we report two novel 3D iron(II)−dicyanoargentate-based coordination polymers, $[Fe(dpb)\{Ag(CN)_2\}\{Ag_2(CN)_3\}]\cdot n$Solv and $[Fe(dpb)_2\{Ag(CN)_2\}_2]$. Two-step SCO versus the HS state in **1**·*n*Solv and **2** are observed and originate from different structural architectures: in-situ generation of $[Ag_2(CN)_3]^-$ and $[Ag(dpb)(CN)_2]^-$ species, respectively; significant argentophilic interactions, and topological networks. Interestingly, **1**·DMF·EtOH and **1**·2DMF·MeCN display two-step guest-effected SCO with hysteresis, accompanying dramatic color changes (HS yellow; LS red). Furthermore, the permanent porosity (299 Å^3 per iron atom) after desolvation of **1**·DMF·EtOH is one of the largest volume values for the Hoffman-like porous SCO coordination polymers to date. In considering the preliminary studies on guest-effected SCO behavior and the large permanent porosity, the solvent-free framework **1** represents a platform for exploring the interplay between host−guest chemistry and SCO behavior. Thus, investigations about SCO properties based on 3D porous SCO coordination polymers and manipulated by various guest molecules are promising.

ASSOCIATED CONTENT

Ⓢ Supporting Information

Selected bond lengths and angles for **1**·DMF·EtOH and **2**, TGA-MS spectra of **1**·2DMF·MeCN, powder X-ray diffraction patterns and TG curve for **1**·*n*Solv, supplementary structural figures for **2**, photographs of **1**·DMF·EtOH; crystallographic data in CIF format. This material is available free of charge via the Internet at http://pubs.acs.org.

AUTHOR INFORMATION

Corresponding Authors

*E-mail: nizhp@mail.sysu.edu.cn.
*E-mail: tongml@mail.sysu.edu.cn.

Notes

The authors declare no competing financial interest.

ACKNOWLEDGMENTS

This work was supported by the "973 Project" (2012CB821704), Program for Changjiang Scholars and Innovative Research Team at the University of China, and NSFC (grant nos. 91122032, 21201182, and 21121061).

REFERENCES

(1) (a) Gütlich, P.; Hauser, A.; Spiering, H. *Angew. Chem., Int. Ed. Engl.* **1994**, *33*, 2024. (b) In *Spin Crossover in Transition Metal Compounds*; Gütlich, P., Goodwin, H. A., Eds.; Topics in Current Chemistry; Springer: Berlin, 2004; Vols. *1*−*3*. (c) In *Spin-Crossover Materials: Properties and Applications*; Murray, K. S., Halcrow, M. A., Eds.; Wiley-VCH: Weinheim, 2013.

(2) (a) Kahn, O.; Martinez, C. J. *Science* **1998**, *279*, 44. (b) Bao, X.; Guo, P.-H.; Liu, W.; Tucek, J.; Zhang, W.-X.; Leng, J.-D.; Chen, X.-M.; Guraslkyi, I.; Salmon, L.; Bousseksou, A.; Tong, M.-L. *Chem. Sci.* **2012**, *3*, 1629.

(3) Létard, J.-F.; Guionneau, P.; Goux-Capes, L. *Top. Curr. Chem.* **2004**, *235*, 221.

(4) Tao, J.; Wei, R.-J.; Huang, R.-B.; Zheng, L.-S. *Chem. Soc. Rev.* **2012**, *41*, 703.

(5) (a) Halder, G. J.; Kepert, C. J.; Moubaraki, B.; Murray, K. S.; Cashion, J. D. *Science* **2002**, *298*, 1762. (b) Muñoz, M. C.; Real, J. A. *Coord. Chem. Rev.* **2011**, *255*, 2068. (c) Liu, W.; Bao, X.; Mao, L.-L.; Tucek, J.; Zboril, R.; Liu, J.-L.; Guo, F.-S.; Ni, Z.-P.; Tong, M.-L. *Chem. Commun.* **2014**, *50*, 4059.

(6) (a) Real, J. A.; Andrés, E.; Muñoz, M. C.; Julve, M.; Granier, T.; Bousseksou, A.; Varret, F. *Science* **1995**, *268*, 265. (b) Neville, S. M.; Moubaraki, B.; Murray, K. S.; Kepert, C. J. *Angew. Chem., Int. Ed.* **2007**, *46*, 2059. (c) Neville, S. M.; Halder, G. J.; Chapman, K. W.; Duriska, M. B.; Southon, P. D.; Cashion, J. D.; Létard, J.-F.; Moubaraki, B.; Murray, K. S.; Kepert, C. J. *J. Am. Chem. Soc.* **2008**, *130*, 2869. (d) Halder, G. J.; Chapman, K. W.; Neville, S. M.; Moubaraki, B.; Murray, K. S.; Létard, J.-F.; Kepert, C. J. *J. Am. Chem. Soc.* **2008**, *130*, 17552. (e) Neville, S. M.; Halder, G. J.; Chapman, K. W.; Duriska, M. B.; Moubaraki, B.; Murray, K. S.; Kepert, C. J. *J. Am. Chem. Soc.* **2009**, *131*, 12106.

(7) (a) Molnár, G.; Cobo, S.; Real, J. A.; Carcenac, F.; Daran, E.; Vieu, C.; Bousseksou, A. *Adv. Mater.* **2007**, *19*, 2163. (b) Southon, P. D.; Liu, L.; Fellows, E. A.; Price, D. J.; Halder, G. J.; Chapman, K. W.; Moubaraki, B.; Murray, K. S.; Létard, J.-F.; Kepert, C. J. *J. Am. Chem. Soc.* **2009**, *131*, 10998. (c) Ohtani, R.; Yoneda, K.; Furukawa, S.; Horike, N.; Kitagawa, S.; Gaspar, A. B.; Muñoz, M. C.; Real, J. A.; Ohba, M. *J. Am. Chem. Soc.* **2011**, *133*, 8600. (d) Muñoz-Lara, F. J.; Gaspar, A. B.; Aravena, D.; Ruiz, E.; Muñoz, M. C.; Ohba, M.; Ohtani, R.; Kitagawa, S.; Real, J. A. *Chem. Commun.* **2012**, *48*, 4686. (e) Sciortino, N. F.; Scherl-Gruenwald, K. R.; Chastanet, G.; Halder, G. J.; Chapman, K. W.; Létard, J.-F.; Kepert, C. J. *Angew. Chem., Int. Ed.* **2012**, *51*, 10154. (f) Muñoz-Lara, F. J.; Gaspar, A. B.; Muñoz, M. C.; Arai, M.; Kitagawa, S.; Ohba, M.; Real, J. A. *Chem.—Eur. J.* **2012**, *18*, 8013. (g) Bao, X.; Shepherd, H. J.; Salmon, L.; Molnár, G.; Tong, M.-L.; Bousseksou, A. *Angew. Chem., Int. Ed.* **2013**, *52*, 1198.

(8) (a) Galet, A.; Niel, V.; Muñoz, M. C.; Real, J. A. *J. Am. Chem. Soc.* **2003**, *125*, 14224. (b) Galet, A.; Muñoz, M. C.; Martínez, V.; Real, J. A. *Chem. Commun.* **2004**, 2268. (c) Arcís-Castillo, Z.; Muñoz, M. C.; Molnár, G.; Bousseksou, A.; Real, J. A. *Chem.—Eur. J.* **2013**, *19*, 6851. (d) Li, J.-Y.; Ni, Z.-P.; Yan, Z.; Zhang, Z.-M.; Chen, Y.-C.; Liu, W.; Tong, M.-L. *CrystEngComm*, **2014**, *16*, DOI:10.1039/C4CE00342J.

(9) Ohba, M.; Yoneda, K.; Agustí, G.; Muñoz, M. C.; Gaspar, A. B.; Real, J. A.; Yamasaki, M.; Ando, H.; Nakao, Y.; Sakaki, S.; Kitagawa, S. *Angew. Chem., Int. Ed.* **2009**, *48*, 4767.

(10) Agustí, G.; Cobo, S.; Gaspar, A. B.; Molnár, G.; Moussa, N. O.; Szilágyi, P. Á.; Pálfi, V.; Vieu, C.; Muñoz, M. C.; Real, J. A.; Bousseksou, A. *Chem. Mater.* **2008**, *20*, 6721.

(11) (a) Bartual-Murgui, C.; Ortega-Villar, N. A.; Shepherd, H. J.; Muñoz, M. C.; Salmon, L.; Molnár, G.; Bousseksou, A.; Real, J. A. *J. Mater. Chem.* **2011**, *21*, 7217. (b) Bartual-Murgui, C.; Salmon, L.; Akou, A.; Ortega-Villar, N. A.; Shepherd, H. J.; Muñoz, M. C.; Molnár, G.; Real, J. A.; Bousseksou, A. *Chem.—Eur. J.* **2012**, *18*, 507.

(12) (a) Niel, V.; Thompson, A. L.; Goeta, A. E.; Enachescu, C.; Hauser, A.; Galet, A.; Muñoz, M. C.; Real, J. A. *Chem.—Eur. J.* **2005**, *11*, 2047. (b) Kosone, T.; Suzuki, Y.; Ono, S.; Kanadani, C.; Saito, T.; Kitazawa, T. *Dalton Trans.* **2010**, *39*, 1786.

(13) Sheldrick, G. M. *SHELXTL97, program for crystal structure refinement*; University of Göttingen: Göttingen, Germany, 1997.

(14) Van Der Sluis, P.; Spek, A. L. *Acta Crystallogr., Sect. A* **1990**, *46*, 194.

(15) Tong, M.-L.; Chen, X.-M.; Batten, S. R. *J. Am. Chem. Soc.* **2003**, *125*, 16170.

(16) Blatov, V. A. *IUCr CompComm Newslett.* **2006**, *7*, 4−38.

(17) (a) Niel, V.; Muñoz, M. C.; Gaspar, A. B.; Galet, A.; Levchenko, G.; Real, J. A. *Chem.—Eur. J.* **2002**, *8*, 2446. (b) Shepherd, H. J.; Bartual-Murgui, C.; Molnár, G.; Real, J. A.; Muñoz, M. C.; Salmon, L.; Bousseksou, A. *New J. Chem.* **2011**, *35*, 1205.

(18) Guionneau, P.; Marchivie, M.; Bravic, G.; Létard, J.-F.; Chasseau, D. *J. Mater. Chem.* **2002**, *12*, 2546.

(19) (a) Moussa, N. O.; Trzop, E.; Mouri, S.; Zein, S.; Molnár, G.; Gaspar, A. B.; Collet, E.; Cointe, M. B.; Real, J. A.; Borshch, S.; Tanaka, K.; Cailleau, H.; Bousseksou, A. *Phys. Rev. B* **2007**, *75*, 054101. (b) Agustí, G.; Muñoz, M. C.; Gaspar, A. B.; Real, J. A. *Inorg. Chem.* **2008**, *47*, 2552. (c) Kosone, T.; Tomori, I.; Kanadani, C.; Saito, T.; Mochida, T.; Kitazawa, T. *Dalton Trans.* **2010**, *39*, 1719.

(20) Chernyshov, D.; Hostettler, M.; Törnroos, K. W.; Bürgi, H.-B. *Angew. Chem., Int. Ed.* **2003**, *42*, 3825.

(21) (a) Tayagaki, T.; Galet, A.; Molnár, G.; Muñoz, M. C.; Zwick, A.; Tanaka, K.; Real, J. A.; Bousseksou, A. *J. Phys. Chem. B* **2005**, *109*, 14859. (b) Bao, X.; Liu, J.-L.; Leng, J.-D.; Lin, Z.-J.; Tong, M.-L.; Nihei, M.; Oshio, H. *Chem.—Eur. J.* **2010**, *16*, 7973.